Biomaterials 131 (2017) 98–110

Contents lists available at ScienceDirect

Biomaterials

journal homepage: www.elsevier.com/locate/biomaterials

Microfluidic-enhanced 3D bioprinting of aligned myoblast-laden hydrogels leads to functionally organized myofibers *in vitro* and *in vivo*

Marco Costantini [a], Stefano Testa [b], Pamela Mozetic [a], Andrea Barbetta [c], Claudia Fuoco [b], Ersilia Fornetti [b], Francesco Tamiro [b], Sergio Bernardini [b], Jakub Jaroszewicz [d], Wojciech Święszkowski [d], Marcella Trombetta [a], Luisa Castagnoli [b], Dror Seliktar [e], Piotr Garstecki [f], Gianni Cesareni [b], Stefano Cannata [b], Alberto Rainer [a, **], Cesare Gargioli [b, *]

[a] Tissue Engineering Lab, Università Campus Bio-Medico di Roma, Rome, Italy
[b] Department of Biology, University of Rome Tor Vergata, Rome, Italy
[c] Department of Chemistry, Sapienza University of Rome, Rome, Italy
[d] Warsaw University of Technology, Faculty of Materials Science and Engineering, Warsaw, Poland
[e] Department of Biomedical Engineering, Techion Institute, Haifa, Israel
[f] Institute of Physical Chemistry, Polish Academy of Sciences, 01224 Warsaw, Poland

ARTICLE INFO

Article history:
Received 16 November 2016
Received in revised form
13 March 2017
Accepted 20 March 2017
Available online 23 March 2017

Keywords:
Microfluidic enhanced 3D bioprinting
Myogenic precursor cells
Myotubes
PEG-Fibrinogen hydrogel
Artificial muscle

ABSTRACT

We present a new strategy for the fabrication of artificial skeletal muscle tissue with functional morphologies based on an innovative 3D bioprinting approach. The methodology is based on a microfluidic printing head coupled to a co-axial needle extruder for high-resolution 3D bioprinting of hydrogel fibers laden with muscle precursor cells (C2C12). To promote myogenic differentiation, we formulated a tailored bioink with a photocurable semi-synthetic biopolymer (PEG-Fibrinogen) encapsulating cells into 3D constructs composed of aligned hydrogel fibers. After 3–5 days of culture, the encapsulated myoblasts started migrating and fusing, forming multinucleated myotubes within the 3D bioprinted fibers. The obtained myotubes showed high degree of alignment along the direction of hydrogel fiber deposition, further revealing maturation, sarcomerogenesis, and functionality. Following subcutaneous implantation in the back of immunocompromised mice, bioprinted constructs generated organized artificial muscle tissue *in vivo*. Finally, we demonstrate that our microfluidic printing head allows to design three dimensional multi-cellular assemblies with an exquisite compartmentalization of the encapsulated cells. Our results demonstrate an enhanced myogenic differentiation with the formation of parallel aligned long-range myotubes. The approach that we report here represents a robust and valid candidate for the fabrication of macroscopic artificial muscle to scale up skeletal muscle tissue engineering for human clinical application.

1. Introduction

In mammalians, myogenesis is a complex phenomenon starting from the very first weeks of embryonic development. This process involves mononucleated cells—named myoblasts—that progressively fuse forming plurinucleated syncytia—named myotubes. As development proceeds, myotubes undergo a maturation process. They grow in size and eventually the actin-myosin based contractile apparatus is assembled, together with the neuromuscular and myotendinous junctions [1].

Skeletal muscles can self-repair relatively small damages resulting from tears, small lacerations, strains, or toxins via a three-stage process that involves demolition, repair, and remodeling of myotubes. However, skeletal muscle cannot restore significant tissue loss that can arise after severe trauma, invasive surgeries, or

* Corresponding author. Department of Biology, University of Rome Tor Vergata, Via della Ricerca Scientifica snc, 00133 Rome, Italy.
** Corresponding author. Tissue Engineering Lab, Università Campus Bio-Medico di Roma, Via Álvaro del Portillo 21, 00128 Rome, Italy.
E-mail addresses: a.rainer@unicampus.it (A. Rainer), cesare.gargioli@uniroma2.it (C. Gargioli).

http://dx.doi.org/10.1016/j.biomaterials.2017.03.026

degenerative diseases [2,3].

Due to the biological and architectural complexity of muscle tissue, engineering an artificial muscle still represents a daunting task. In the recent past, few strategies have been proposed to generate skeletal muscle tissue *in vitro* [4–6] and *in vivo* [7,8]. In most studies, researchers primarily focused on the obtainment of highly oriented myotubes that could mirror the natural organization of muscle fascicles, by inducing either a mechanical—static or dynamic—or electrical stimulation. These methods demonstrated the possibility of obtaining highly oriented myofibers, but showed limitations in terms of process scalability. In addition, the goal of achieving a multicellular spatially organized structure, mimicking the complexity of native muscle, has not been fully addressed. Finally, most of these studies rely on bulk cell-laden hydrogels, that hinder the formation of aligned myotubes, as it has been proved that, in such conditions [7,9], muscle precursor cells create a chaotic 3D entangled network of myotubes similar to those obtained in 2D cultures. Hence, it is of utmost importance to develop alternative approaches for improved *ex vivo* fabrication of muscle tissue that would ultimately be suitable for organ transplantation *in vivo*.

3D bioprinting has the potential to fabricate highly customizable and highly organized structures that, in principle, could be used for the assembly of an entire muscle [10–12]. This emerging biofabrication technology relies on the simultaneous deposition of cells and biomaterials in a layer-by-layer fashion, to form 3D well-organized heterogeneous structures that can mirror relevant complex biological architectures both physiologically and morphologically. Thanks to these attractive features, 3D bioprinting is rapidly becoming a first-choice technique for a broad set of tissue engineering (TE) scenarios, including skeletal muscle tissue reconstruction [13–15]. In these approaches, hydrogels containing muscle precursor cells are deposited in combination with support structures in thermoplasts (e.g., polycaprolactone [13,15], polyurethane [15]) and/or sacrificial materials (e.g., Pluronic F127 [14]) to achieve proper arrangement of cell-laden struts. It was noticed, however, that the level of organization of differentiated muscle precursor cells—*i.e.*, the formation of long-range multinucleated myotubes, their degree of alignment, and the assembly of sarcomeres—was limited, most likely due to substrate mechanical properties and matrix density issues.

Inspired by the native structural morphology of skeletal muscles, we speculated that the spatial confinement of muscle precursor cells into highly aligned and compact 3D bioprinted hydrogel fiber structures could lead to a better orientation of the arising myotubes, thus mimicking the natural muscle morphology and organization more closely. Building on such a premise, we developed a 3D bioprinting strategy based on a custom microfluidic printing head coupled to a co-axial extruder. This system enables high resolution multi-material and multi-cellular deposition by simultaneously extruding different bioinks or by rapidly switching from one bioink to another. In this report, we first demonstrate that, within few days of *in vitro* culture following 3D bioprinting, muscle precursor cells start to elongate and fuse, forming highly aligned myotubes. This is followed by a thorough analysis of the obtained artificial myo-structures in terms of myotube length and orientation, fluorescence immunocytochemistry, and gene expression of relevant myogenic differentiation markers. Then, we demonstrate *in vivo* that the 3D bioprinted constructs outperform control bulk-hydrogels in terms of myotube structural organization, supporting the hypothesis that the simple geometrical confinement exerted by 3D bioprinted hydrogel fibers promotes the architectural organization of muscle precursors cells. Finally, we exploit the microfluidic printing head to assemble 3D structures containing spatially organized combinations of different cell types. We demonstrate that, through the implementation of a microfluidic platform as the printing head, it is possible to achieve a level of accuracy that was previously unachievable in extrusion-based systems.

2. Materials and methods

2.1. Materials

All chemicals were purchased from Sigma-Aldrich and used without further purification unless otherwise stated. Sodium alginate (ALG, $M_w \approx 33$ kDa) was a kind gift from FMC Biopolymers.

2.2. Synthesis of photocurable PEG-Fibrinogen

Photocurable PEG-Fibrinogen (PF) was synthesized according to a previously published two-step synthetic route [16]. Fibrinogen molecules were first cleaved into smaller fragments in a 70% formic acid solution containing 17 mg/mL cyanogen bromide (CNBr). After dialysis purification, these fragments were pre-treated with Tris(2-carboxyethyl) phosphine hydrochloride (TCEP, molar ratio TCEP/fibrinogen cysteines = 68:1) in a 50 mM PBS solution containing 8 M urea to reduce disulfide bonds to thiol groups and then reacted with PEG-diacrylate (M_w = 20 kDa, 250 mg/mL) following a thiol-ene Michael addition. Thus, a photocurable semi-synthetic polymer was obtained, composed of fibrinogen denatured fragments with covalently-attached PEG side chains bringing a vinyl moiety at their extremities. After purification, PF was redissolved, sterile filtered and stored at −80 °C as a stock solution.

2.3. Bioink formulation

ALG stock solution was prepared at a concentration of 100 mg/mL in HEPES 62.5 mM. In a typical bioink preparation, 400 μL of ALG solution were mixed with 600 μL of freshly thawed PF stock solution, leading to a final concentration of 8 mg/mL PF, 40 mg/mL ALG. Irgacure 2959 (BASF) was then added as a radical photoinitiator at a final concentration of 1 mg/mL.

The two biopolymers—PF and ALG—used for the formulation of the bioink played different roles in the presented 3D bioprinting experiments: ALG was used only as temporary templating material to allow a precise deposition of cell-laden hydrogel fibers through a custom-built co-axial printing head, simultaneously delivering the bioink and a cross-linking solution of $CaCl_2$, while PF, after UV curing, generated a covalently cross-linked matrix into which embedded myoblast could spread and differentiate.

The relative concentration of ALG and Ca^{+2} ions have been optimized in previously published works [17,18] through a systematic screening to guarantee both a cell-friendly environment and high accuracy and resolution of 3D-printed structures.

2.4. Bioink rheology

Steady and dynamic rheological characterization of the polymeric solutions was performed at 23 °C on an Anton Paar MCR-302 rheometer equipped with a cone-plate system (diameter = 40 mm, angle = 1°).

The viscoelastic properties, storage modulus $G'(\omega)$ and loss modulus $G''(\omega)$ were determined through small amplitude oscillating shear flows at angular frequencies ranging from 10^{-1} to 10^{2} rad/s. Strain sweep experiments were performed first to determine the linear strain regime. Shear viscosity behavior of the bioinks was evaluated by applying a shear rate from 0.01 to 100 s^{-1}. Both steady shear and dynamic measurements were carried out as

a function of ageing time. PF solution, stored at −80 °C, was rapidly thawed and brought to room temperature. Immediately after, it was diluted with either HEPES buffer (PF group) or 10 wt% alginate in HEPES (PF-ALG group) to a final concentration of 0.8 wt% (ALG concentration 4 wt%) and gently stirred for 5 min. The solution was then poured on the plate of the rheometer which was set at 23 °C, and allowed to thermally equilibrate for 60 s prior to starting the measurement. This time point was conventionally chosen as the zero value for the ageing time.

2.5. Design and fabrication of the microfluidic printing head

The dispensing head was purposely designed to be compatible with multi-material deposition and rapid switch among different bioinks. The system was obtained by combining a microfluidic chip bearing a Y-junction (2 inlets, 1 outlet) with a coaxial needle system. The microfluidic device was fabricated by micro-milling, engraving microfluidic channels into two 5-mm-thick polycarbonate sheets. After machining, the two sheets were sonicated in isopropanol for 30 min and then sealed with a hot press at 130 °C for ca. 30 min. All channels were milled with a 200 × 200 μm cross-section. The chip outlet was fluidically connected to the inner needle (25 G) of the coaxial needle system, while the outer needle (19 G) presented an independent side inlet and was mounted coaxially with the inner needle.

A gantry system based on precision linear stages (PI miCos PL-S series, controlled by Galil DMC-1840 motion controller) was purposely assembled and positioned inside a Class II biological safety cabinet. The microfluidic head was coupled to the motorized gantry system, and its inlets connected to microfluidic syringe pumps (neMESYS low pressure, Cetoni GmbH) by autoclavable Teflon tubing (ID 1/16″).

2.6. Fabrication of 3D bioprinted constructs

Bioink was laden with C2C12 myoblasts (ATCC) at a density in the $1 \div 5 \times 10^7$ cells/mL range and supplied to the inner needle of the dispensing coaxial system, while the outer needle was fed with calcium chloride solution (0.3 M). The printing speed, as well as the flow rates of the bioink and crosslinking solutions were adjusted to obtain hydrogel fibers ≈ 250 μm in diameter (printing speed = 180 mm/min, $Q_{bioink} = 5$ μL/min, $Q_{Ca^{2+}} = 4.6$ μL/min). For all the experiments, the layer height was set to 120 μm, the distance between hydrogel fibers in the X-Y plane to 50 μm, and a total of 7 layers were manufactured (corresponding to ca. 1.5×10^6 cells/construct), with an aligned organization of fibers to mimic the natural morphology of muscle tissue.

Bulk-hydrogel constructs were fabricated as a negative control group by casting the bioink on a rectangular mold (approx. equal in size to the 3D bioprinted constructs), followed by crosslinking with 0.3 M calcium chloride solution.

Constructs (both 3D bioprinted and bulk-hydrogel) were crosslinked by low-dose UV irradiation (365 nm, 1.3 mW/cm^2 for 5 min), washed with 25 mM HEPES buffer containing 20 mM EDTA for 5 min, and finally forwarded to *in vitro* and *in vivo* experiments.

As a proof of concept, the fabrication of multi-cellular constructs containing two different cell types was also carried out. Bioink was laden with either C2C12 or BALB/3T3 (infected with GFP and mOrange, respectively) at the same cell density of 2×10^7 cells/mL. The two resulting cell-laden bioinks were fed through the two inlets of the Y-junction of the printing head at the same flow rate ($Q_{C2C12} = Q_{BALB/3T3} = 2.5$ μL/min), and bioprinting process was performed as above described.

2.7. Microcomputed tomography - μCT

Acquisition of 3D bioprinted morphologies was performed by micro-computed tomography (μCT) on acellular specimens. Prior to scanning, samples were partially dried in 50% ethanol for 5 min and then dipped into sunflower oil to increase X-ray contrast. Scanning was performed using an Xradia MicroXCT-400 with the following parameters: 40 kV voltage, 10 W power, no filter material, 0.18° rotation step in an angle interval of 184°. Voxel size was $4.97 \times 4.97 \times 4.97$ μm^3. Image analysis and 3D reconstruction of printed samples were performed with ImageJ software [19].

2.8. In vitro culture of 3D bioprinted constructs

3D bioprinted constructs were cultured up to 21 days in DMEM (Gibco) supplemented with 10% heat-inactivated fetal bovine serum (FBS, Gibco), 100 IU/mL penicillin and 100 mg/mL streptomycin (Gibco) at 37 °C and 5% CO_2 humid atmosphere. The same conditions were also employed during *in vitro* culture of C2C12-laden bulk-hydrogel constructs.

2.9. In vivo construct implantation

Following 7 days of *in vitro* culture, 3D bioprinted and bulk-hydrogel constructs were implanted subcutaneously in the back of immunocompromised mice. Two-month-old male SCID mice (n = 5) were anesthetized with a 1:1 mixture of ketamine (5 mg/mL) and xylazine (1 mg/mL) at a dose of 10 mL/kg i.m. Following a limited skin incision on the medial side of the back, dorsal muscle was separated from the skin, the construct was carefully positioned and skin closure was performed by non-absorbable 6-0 silk sutures (Clinsilk). Mice were sacrificed at 28 days after implantation for morphological analysis. All experiments involving animals were conducted according to the protocols of good animal experimentation under the Italian Health Minister approval n° 228/2015-PR.

2.10. Immunofluorescence

Following *in vitro* culture, 3D bioprinted and bulk-hydrogel specimens were fixed in 2% PFA and processed for fluorescence microscopy as previously described [20]. Conversely, constructs explanted from SCID mice were embedded in O.C.T. and quickly frozen in liquid nitrogen cooled isopentane for sectioning at a thickness of 8 μm on a Leica cryostat. Sections were rehydrated in PBS and permeabilized with 0.2% Triton X-100 in PBS for 30 min. Sections were incubated with anti-Myosin Heavy Chain (MHC, Clone MF20 DSHB, 1:2 titer) and rabbit anti-Laminin (LAM, Sigma-Aldrich #L9393, 1:500) primary antibodies in blocking buffer (PBS plus 0.2% Triton X-100 and 20% heat-inactivated goat serum) for 1 h at room temperature (RT). After several washes with PBS, sections were incubated with anti-mouse FITC (Chemicon, 1:500) and anti-rabbit Alexa488 (Molecular Probes, 1:500) secondary antibodies in blocking buffer for 1 h at RT. Samples were counterstained with DAPI to detect nuclei, washed 3 times with PBS, and mounted on glass slides with Vectashield mounting medium (Vector Laboratories). Samples were imaged with a Nikon Eclipse TE2000 microscope equipped with a CoolSNAP MYO CCD camera (Photometrix) and MetaMorph software.

2.11. Total RNA isolation and RT-qPCR analysis

Expression levels of myogenic genes were evaluated on 3D bioprinted and bulk-hydrogel constructs following *in vitro* culture by two-step Quantitative Reverse Transcription PCR (RT-qPCR). Total RNA was extracted and isolated using TRI Reagent (Sigma-

Aldrich). Extracted mRNA was quantified by spectrophotometric technique (Tecan Infinite M200 Pro) and 1 μg of total RNA was reverse-transcribed using High Capacity cDNA Reverse Transcription Kit (Thermo Fisher Scientific) according to the manufacturer's protocol. Quantitative PCR analysis was performed on 10 ng of cDNA in a total reaction volume of 10 μL, using TaqMan Universal MasterMix II (Thermo Fisher Scientific) and primers (TaqMan Gene Expression Assay, Thermo Fisher Scientific) for the following genes: mouse myogenic differentiation 1 (MyoD1, Mm00440387_m1), sarcomeric actin (ACTA1, Mm00808218_g1), myogenin (MYOG, Mm00446195_g1), and myosin heavy chain 2 (MYH2, Mm01332564_m1). In order to identify the best housekeeping gene, analysis of the expression levels of several candidate reference genes was performed. In particular, after verifying the stability of hypoxanthine phosphoribosyltransferase (HPRT, Mm01318747_g1), TATA-binding protein (TBP, Mm00446971_m1), casein kinase 2 (Csnk2a2, Mm01243455_m1), adaptor related protein complex 3 delta 1 subunit (AP3D1, Mm00475961_m1) and peptidylprolyl isomerase A (PPIA, Mm02342429_g1) using geNorm v.3.5 [21], AP3D1 was chosen as the endogenous control. All experiments were performed in triplicate.

2.12. Image analysis

Image analysis was performed using ImageJ software. In particular, the distribution of myotube length and orientation on 3D bioprinted constructs following *in vitro* culture was obtained from immunofluorescence micrographs by manually skeletonizing myotubes into polylines. Myotube length was obtained as the sum of all the segments composing each polyline, while myotube orientation was calculated as the weighted average of the angle formed by each segment with the direction of hydrogel fiber deposition (0°), weighted by its length.

Analysis of inter-myofiber space was performed on immunostained explant tissue sections. Briefly, LAM staining was used to extract the contours of each myotube and to create a mask for the generation of binary images, to which *Local Thickness* and *3D Color Inspector* plugins were applied. Color-maps data were further processed to generate a pixel-based distribution plot of inter-myofibers spacing [22].

3. Results

3.1. Microfluidic printing head, bioink formulation and rheology

As an emerging biofabrication field, 3D bioprinting still presents some criticalities. Two of the biggest challenges, which hamper the progress in this field and its translation toward the clinical arena, relate to i) the formulation of bioinks and ii) the possibility to perform the deposition multi-material/cellular structures within a single construct [23,24]. To address all of these challenges, we employed a microfluidic bioprinting head (Fig. 1a–c) featuring a multi-inlet Y-junction feeding a co-axial needle. The system was characterized by overall small dimensions of the channels (200 × 200 μm cross-section, dead volume < 1.5 μL), compatible with rapid composition switching. Furthermore, since the system operated in a laminar regime (Re ≈ 6×10^{-3} in our printing conditions), deposition of hydrogel fibers with an exquisitely tailored spatiotemporal composition could be performed.

The instantaneous gelation of the bioinks took place at the tip of the inner needle, where the bioinks delivered from the microfluidic device came into contact with the cross-linking solution supplied through the external needle (Fig. 1c). This was achieved by exploiting the property of alginate to undergo instantaneous gelation when exposed to divalent calcium ions. Such instantaneous gelation prevented hydrogel fibers from collapsing, leading to extremely high accuracy and shape fidelity of the 3D bioprinted structures [25] (see supplementary video of 3D printing).

Supplementary video related to this article can be found at http://dx.doi.org/10.1016/j.biomaterials.2017.03.026.

In this work, we chose to blend ALG with a semi-synthetic biopolymer (PF), consisting of fibrinogen fragments with covalently-attached PEG side chains bringing a vinyl moiety at their ends.

A fundamental property of fibrinogen is its ability to self-assemble into non-covalent networks, as in the first steps of wound healing. While crucial from a biological point of view, this phenomenon may represent an obstacle in the use of fibrinogen as a biomaterial, in particular for 3D bioprinting applications. Indeed, the presented 3D bioprinting method requires fluid solutions in order to maintain resolution and shape fidelity constant during printing. To assess whether PF still exhibited the tendency of pristine fibrinogen to self-assemble, eventually giving rise to a gel, a detailed rheological characterization was carried out: the evolution of the storage (G') and loss (G'') moduli for increasing ageing times is reported in Fig. 2a. Already at early time points (0 and 3 min), the presence of some degree of supramolecular organization was confirmed by the analysis of G′ and G″ traces, with G″ being lower than G′ at low shear rate values (*i.e.,* the viscous region). At longer ageing times, a clear tendency of PF chains to organize into a network was reported. After 10 min a weak gel-like behavior was evidenced, and for longer ageing times (20 min) the network structure consolidated further, as witnessed by the enhanced separation between G' and G'' traces. The gel could be categorized as a weak one, since both G' and G'' displayed a marked dependence on the frequency [26]. This information is valuable, since it provides a practical criterion for the timing and handling conditions of PF solutions. The rheological data indicated that PF solutions had to be used within the very few minutes after thawing.

The use of the above described microfluidic printing head relies on the ionic gelling properties of alginate, meaning that PF must be blended with alginate (PF-ALG). Therefore, characterization of PF-ALG was performed in a similar fashion to verify whether the addition of alginate attenuated the effects of ageing. Results are reported in Fig. 2d, where data for pristine ALG have also been included. The most relevant aspect is that the blend did not exhibit any time dependent behavior, with G' and G'' traces not changing significantly on a time scale of 20 min. Furthermore, we studied the possible occurrence of time dependent phenomena regarding viscosity (η) and shear stress (τ). Again, the analysis was carried out in a comparative fashion by taking into consideration PF and the PF-ALG blend. A pronounced shear thinning behavior as a function of $\dot{\gamma}$ was observed in both cases (Fig. 2, b c, e, f). As a reference, we also report the viscosity of a solution of pristine ALG (green circles in Fig. 2e), the behavior of which was essentially Newtonian. The most relevant difference between the two datasets was the time invariant behavior of η and τ for PF-ALG at $\dot{\gamma}$ values above 10 s^{-1}, while PF exhibited a quite pronounced dependence on the ageing time in the whole range of shear rate. By entering this value into the shear stress vs. shear rate plot (Fig. 2f), it was possible to extrapolate a critical shear stress value of ≈1.3 Pa above which the bioink was substantially unaffected by ageing.

3.2. Optimization of 3D bioprinting process

The role of the microarchitecture—i.e., fiber orientation and fiber-to-fiber distance—on the performance of bioprinted constructs has been addressed by relatively few works [27,28], while the majority of the approaches still rely on the common alternating

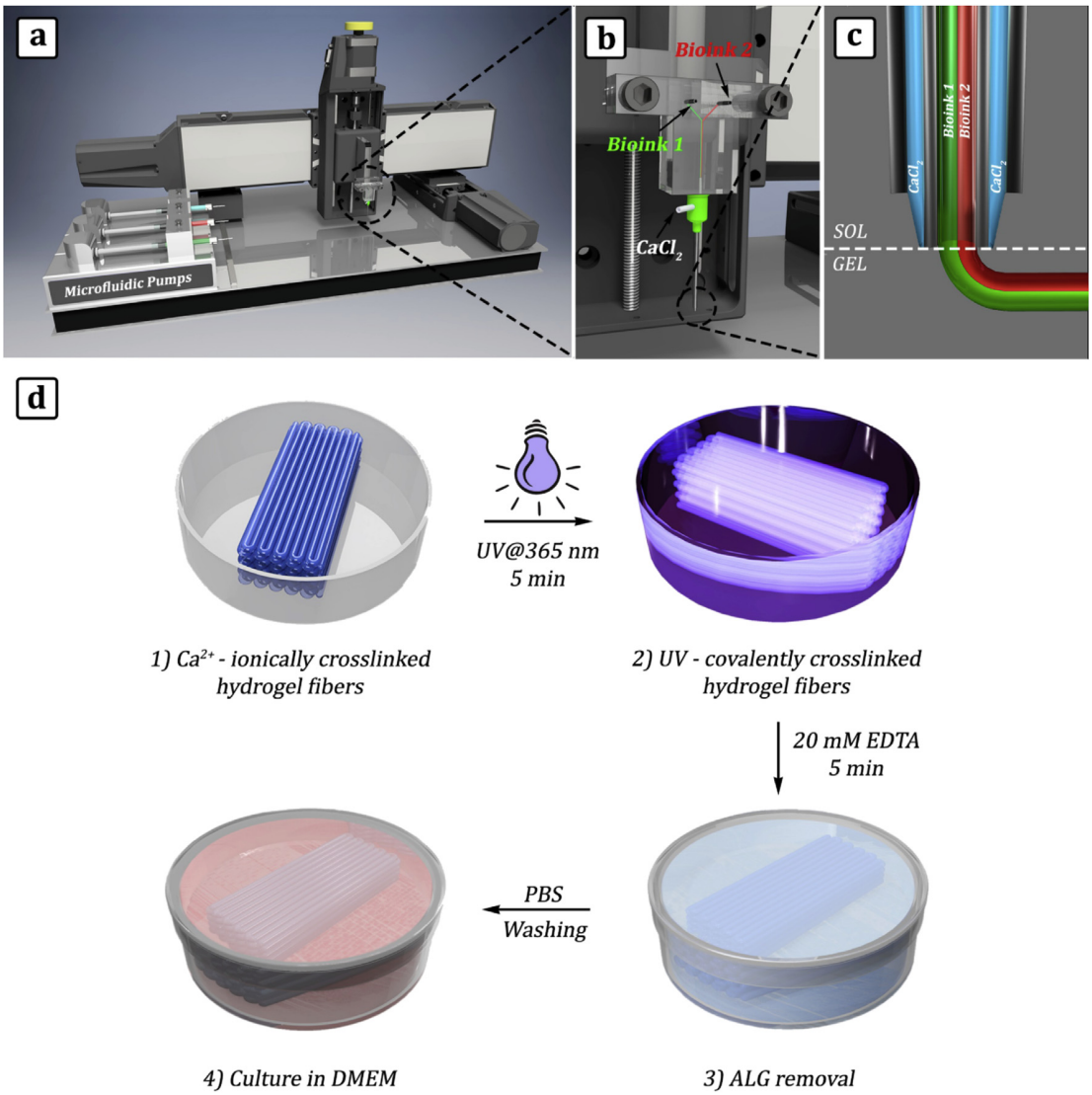

Fig. 1. 3D bioprinting set-up. a) Custom-built 3D printer equipped with fully programmable microfluidic pumps. b) Microfluidic printing head coupled to (c) coaxial extruder. d) Diagram showing the procedure for the fabrication of covalently crosslinked 3D bioprinted PEG-Fibrinogen based scaffolds and the following ALG removal prior to undergo *in vitro* culture.

0–90° pattern as a volume-filling strategy. Although this architecture may be generally sufficient for most applications, the 3D deposition of muscle precursor cells should take into account the high degree of anisotropy of the target tissue (see Supplementary Fig. S1).

For this reason, we chose to better mimic the native morphology of skeletal muscles by designing a toolpath for the deposition of layers of aligned fibers. Compared to the common 0–90°, such an architecture is less mechanically stiff as the number of junction points among fibers belonging to adjacent layers is drastically reduced. To account for such potential limitation, a careful optimization of printing parameters was carried out. We restrained from the common strategies used to improve the stability of additively manufactured structures, and consisting in the deposition of either additional adhesion layers—generally at the beginning of the printing process—or a perimetric shell to confine the desired structure. Either of these strategies are not suitable for our purpose, as they partially reduce the degree of biomimicry of the engineered constructs. Instead, we managed to stabilize the deposition of purely aligned fibers by i) minimizing the distance among laying fibers in X-Y plane (down to ~ 50 μm) and ii) shifting the fibers of each new layer, so that the center of each fiber fell midway between the underlying fibers. Although not fully reaching close cylinder packing configuration (*i.e.*, honeycomb lattice with kissing number = 6 and packing density = 0.9069), the contact area among fibers was greatly augmented and specimens showed prolonged structural integrity and stability in culture medium after PF photo-crosslinking (Fig. 3).

Another parameter that required careful optimization was the cell density in the bioink (see Supplementary Fig. S2). In fact, to undergo a rapid and efficient fusion and differentiation in 3D, muscle precursor cells require intimate cell-to-cell contact within the hydrogel [29]. We thus performed a series of experiments with different cell densities in the $1 \div 5 \times 10^7$ cells/mL range, with best performances achieved for a cell density ca. 2×10^7 cells/mL. At lower cell densities ($<2 \times 10^7$ cells/mL), myotube formation was

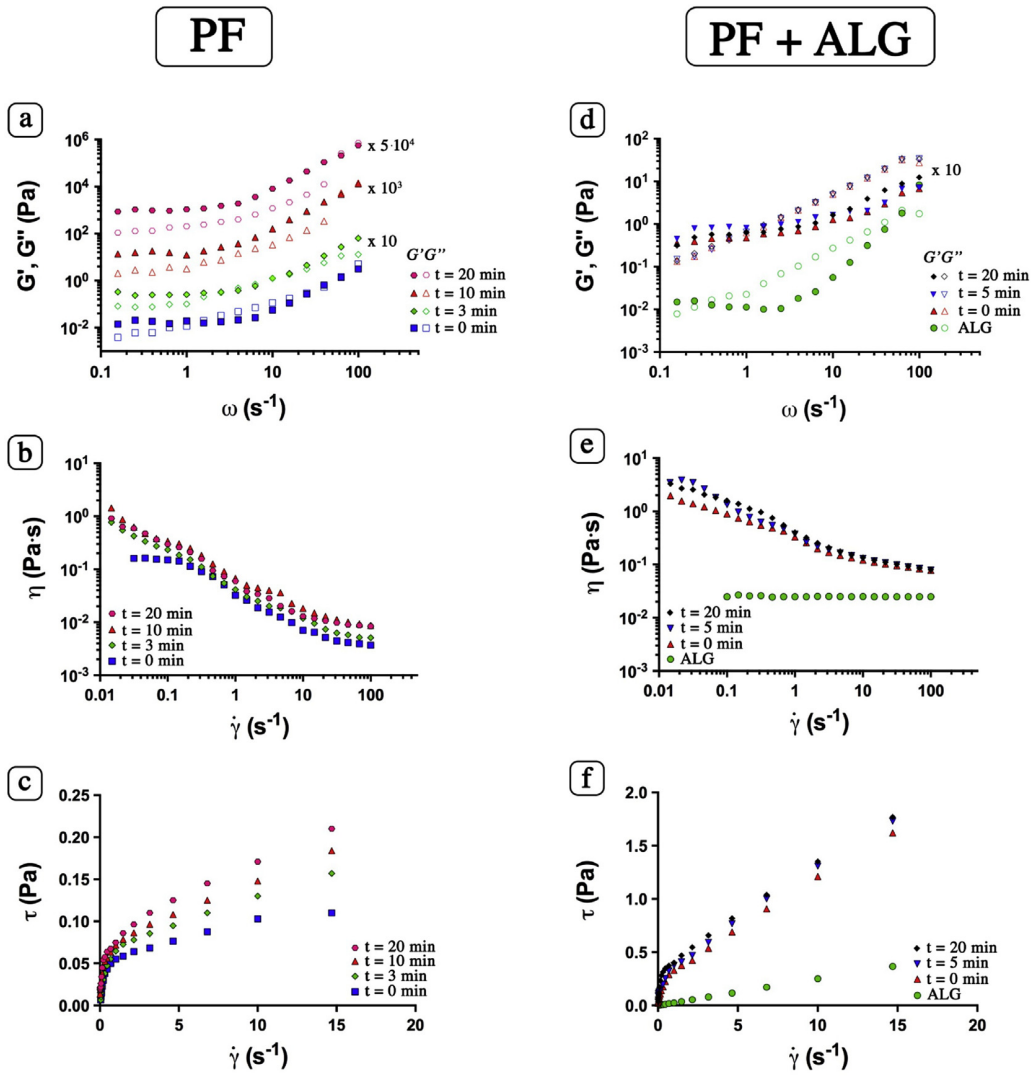

Fig. 2. Rheological studies. a-c) PF (0.8% w/w) d-f) PF (0.8% w/w) + ALG (4% w/w) in 25 mM HEPES buffer at different ageing times as indicated in the graphs. a, d) Storage (G', filled symbols) and loss (G'', empty symbols) moduli. Shear rate dependencies: b, e) viscosity (η) c, f) shear stress (τ). Curves were scaled along the vertical axes by the multiplying factors indicated in graphs in a) and d).

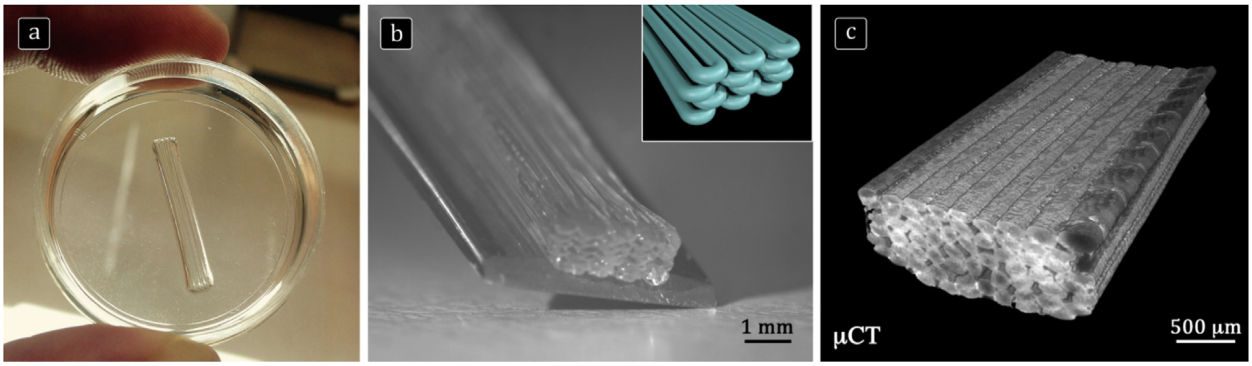

Fig. 3. a) 3D bioprinted structure composed of unidirectional aligned PF hydrogel fibers. a) Macrograph of a 3D bioprinted construct into a 35 mm Petri dish. b) High magnification optical micrograph of the construct; a schematic representation of fiber arrangement is reported in the inset. c) X-ray microtomographic scan of the sample in (a).

hampered, most likely due to the increased distance between neighboring cells. Higher cell densities (>3 × 10^7 cells/mL), on the contrary, led to the formation of unorganized cell clusters, that hindered proper cell elongation and differentiation.

The last key parameter that influenced the number and quality of myotubes was the hydrogel stiffness. It is well known that myoblasts *in vitro* sense the substrate stiffness which, in turn, affects cell differentiation and sarcomeric unit assembly [30]. In the presented approach, after 3D bioprinting and UV-crosslinking, the deposited hydrogel fibers were composed of an interpenetrating polymer network (IPN) of ionically crosslinked ALG and chemically crosslinked PF chains. The Young's modulus of such IPN system (48 kPa) was well above the optimal range of substrate modulus for myotube differentiation (8–11 kPa) [30,31], with the ionically crosslinked ALG network contributing for the most part to the overall stiffness. However, ALG network could be easily disassembled by exposure to solutions containing calcium chelating agents, such as EDTA (see Supplementary Fig. S3). Once optimized, this process could be systematically used to control the stiffness of the constructs and bring it to values more suitable for myotube differentiation. We found that a good compromise between cell viability, construct stability, and myotube differentiation was obtained with 5 min washing in 20 mM EDTA solution.

3.3. In vitro culture of 3D bioprinted myostructure

We fabricated highly aligned hydrogel structures laden with C2C12 at a concentration of 2 × 10^7 cells/mL. In parallel, we prepared PF bulk-hydrogels with the same myoblast cell density. Micrographs confirmed that, within 24/48 h after polymerization, bulk-hydrogels quickly undertook myogenic differentiation forming a chaotic 3D entangled network of myotubes (Figs. S4a and b), in agreement with already published data [7,32]. Similarly, myoblasts in the 3D bioprinted constructs showed a remarkable muscle differentiation, albeit with a small delay. Differently from myotubes in the bulk-hydrogel, those in the printed constructs displayed a striking parallel organization, accompanied by the expression of MHC and LAM (a component of the basal lamina of muscle fibers), as it naturally occurs in skeletal muscle (Figs. S4c and d). The muscle differentiation process was monitored up to 21 days, studying the 3D bioprinted myo-structure every 4 days by bright field and immunofluorescence microscopy (Fig. 4). Micrographs documented an increase in myotube number and length with increasing culture time, and this was accompanied by an increase in MHC expression. Since the initial days of culture, myoblasts started migrating, spreading, differentiating and fusing, forming multinucleated myotubes within the 3D bioprinted fibers. Interestingly, muscle precursor cells elongated in the direction of fiber deposition, before fusing with adjacent cells. This may be rationalized as polymeric chains orienting in the direction of flow upon extrusion, and cells sensing an anisotropic surrounding matrix.

At late time points (12, 16 and 21 days after printing), myotubes underwent sarcomerogenesis as revealed by higher magnification immunofluorescence micrographs. At day 21, completely striated myofibers were observed (Fig. 4i–o, white arrows). The assembly of sarcomeres, besides being considered the gold standard marker of advanced myotube maturation, guarantees their proper contractile function (see supplementary video of spontaneous contracting myostructures).

Supplementary video related to this article can be found at http://dx.doi.org/10.1016/j.biomaterials.2017.03.026.

To gain a quantitative overview of the differentiation status of C2C12 myoblasts, we analyzed the gene expression of relevant myogenic differentiation markers (ACTA1, MyoD1, MYOG, MYH2—Fig. 5). Results further confirmed the muscle differentiation progress in relation with culture time and with myostructure maturation, with an exceptional expression of MYH2 that was approximately 5000 times higher than at day 0.

Finally, we evaluated the degree of myotube alignment and length in muscle networks obtained in 3D bioprinted constructs. These are two important parameters that influence the functionality of the engineered tissue. We thus analyzed a quite large region (2000 × 300 μm) of a 3D bioprinted construct after 15 days of *in vitro* culture. Immunofluorescence analysis showed a strong myogenic differentiation, as evidenced by multinuclear syncytia formation and MHC expression (Fig. 6a and b). Quantitative image analysis revealed a larger fraction of long myotubes in the range 300–400 μm (average myotube length = 346 μm) with a highly parallel orientation (>90% myotubes within ±10° deviation vs. fiber printing direction, Fig. 6c–d), confirming that 3D bioprinting represents an ideal approach for the fabrication of macroscopic artificial skeletal muscles.

3.4. In vivo grafting of 3D bioprinted myostructure

To study whether the 3D bioprinted structures have the potential to mature into functional muscle tissue *in vivo*, we implanted them subcutaneously on the back of immunocompromised SCID mice (Fig. 6). In order to elute the ALG component, scaffolds were pre-cultured *in vitro* for 7 days, a time period that is not sufficient to obtain mature myotubes (Fig. 4), prior to *in vivo* implantation. Similarly, we also implanted PF bulk-hydrogel—containing C2C12 myogenic progenitors at a comparable density—to better assess the potential beneficial effect of 3D bioprinting approach.

The implants were collected and analyzed 28 days after grafting, macroscopically revealing the formation of a “pinkish” tissue like structure (Fig. 7a,b). Histological analysis performed on bulk-hydrogel and 3D bioprinted implants revealed the formation of artificial muscle like tissue composed by MHC-positive myofibers surrounded by LAM in both implant types (Fig. 7c,d,e,h). However, 3D bioprinted implants were characterized by a more pronounced parallel orientation and organization, with a uniform size of muscle fibers (Fig. 7e,h). In addition, they showed denser myofiber organization with reduced inter-fiber spacing (compare Fig. 7f,g with Fig. 7i,j). Interestingly, 3D bioprinted hydrogel fibers were partially degraded (Fig. 6d) after 28 days *in vivo*, and partially substituted by the arising myofibers.

Finally, 3D bioprinted explants were further sectioned longitudinally (Fig. 7k,m) to evaluate the myofiber differentiation status. After 28 days *in vivo*, completely striated myofibers were observed, confirming the advanced degree of myotube maturation.

3.5. Multi-cellular 3D bioprinting via microfluidic printing head

As a proof of concept, we tested the performance of our microfluidic printing head in the fabrication of multi-cellular 3D bioprinted scaffolds containing two different cell types—namely C2C12 and BALB/3T3 (Fig. 8). The benefits of co-culturing myoblasts (C2C12) with fibroblasts (BALB/3T3) has been reported in the past, demonstrating that fibroblasts support myoblast differentiation by secreting extracellular matrix components and growth factors [33]. Fluorescence micrographs suggested that C2C12 and BALB/3T3 were finely compartmentalized within the deposited hydrogel fibers and that the Janus flow pattern formed in the outlet channel of the microfluidic printing head was perfectly retained following gelation (Fig. 8b). Interestingly, after 5 days of culture, C2C12 started to spread and fuse, forming myotubes exclusively on the side of the hydrogel fibers in which they were compartmentalized (Fig. 8c).

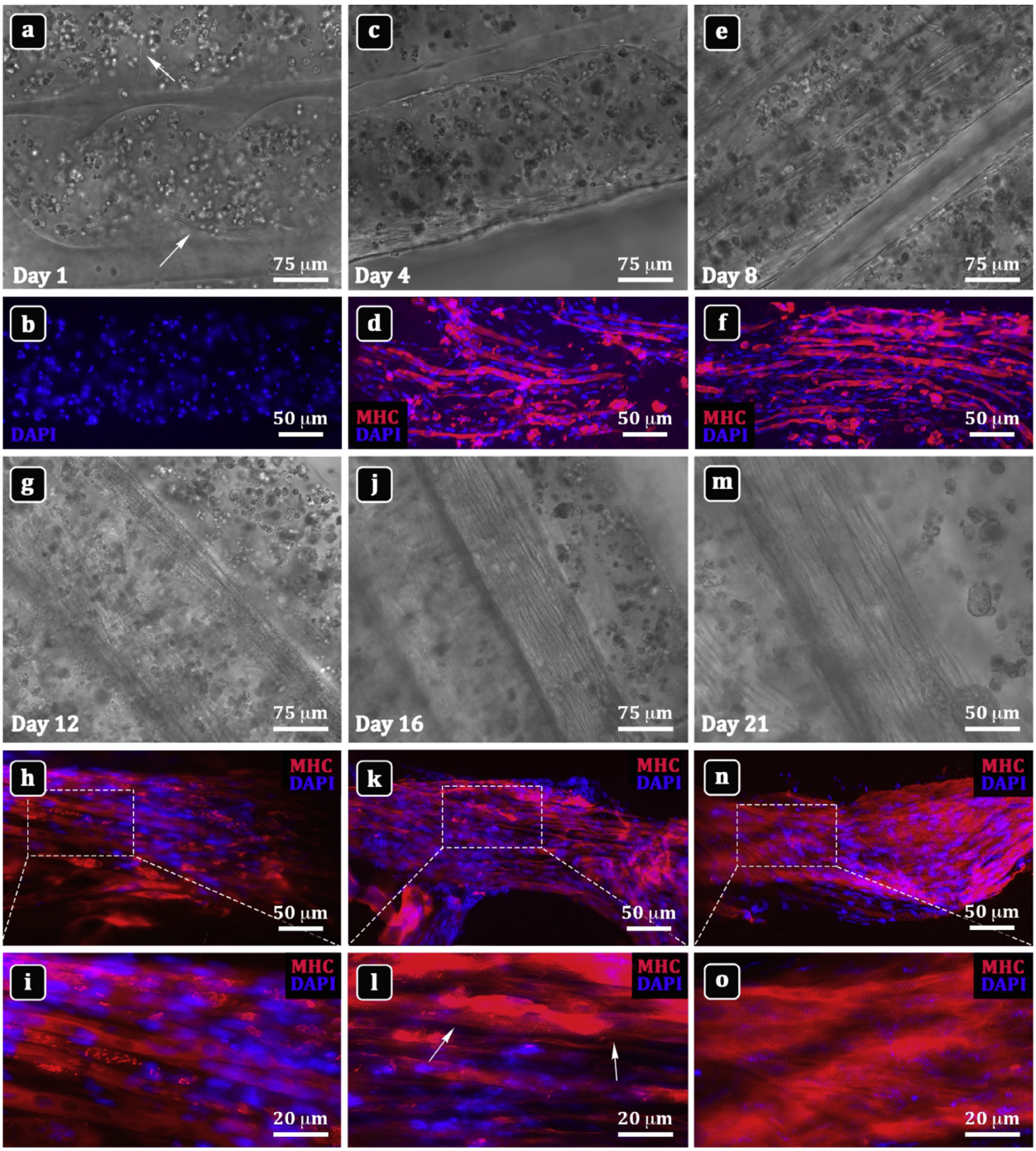

Fig. 4. Bright field and MHC immunofluorescence micrographs of 3D bioprinted C2C12 myogenic cells at different time points. a,b) Day 1 showing round shaped, MHC negative C2C12 cells. c,d) Day 4 displaying myogenic differentiation besides MHC expression. e,f) Day 8 revealing increasing formation of myotubes expressing MHC; g-i) Day 12 presenting close packing of aligned myotubes. j-l) Day 16 showing a well-organized myostructure with the first evidence of sarcomere formation (white arrows) m-o) Day 21 revealing the progressive formation of myofibers and an outstanding sarcomeric organization. Nuclei were counterstained with DAPI.

4. Discussion

Skeletal muscle tissue engineering represents an emerging field that holds great promise for assembling artificial muscles to be used for *ex vivo* studies and eventually for the replacement of diseased or injured muscle tissue. To date, however, none of the numerous strategies that have been proposed proved completely satisfactory [34–36]. Although these methods were developed with great expectations for their possible therapeutic applications, so far the results achieved *in vivo* are scarce [37–39]. Mirroring the natural structural organization of parallel-oriented myofibers has been one of the major difficulties encountered. A number of different approaches have demonstrated encouraging effect on myostructure organization, promoting muscle fibers alignment and

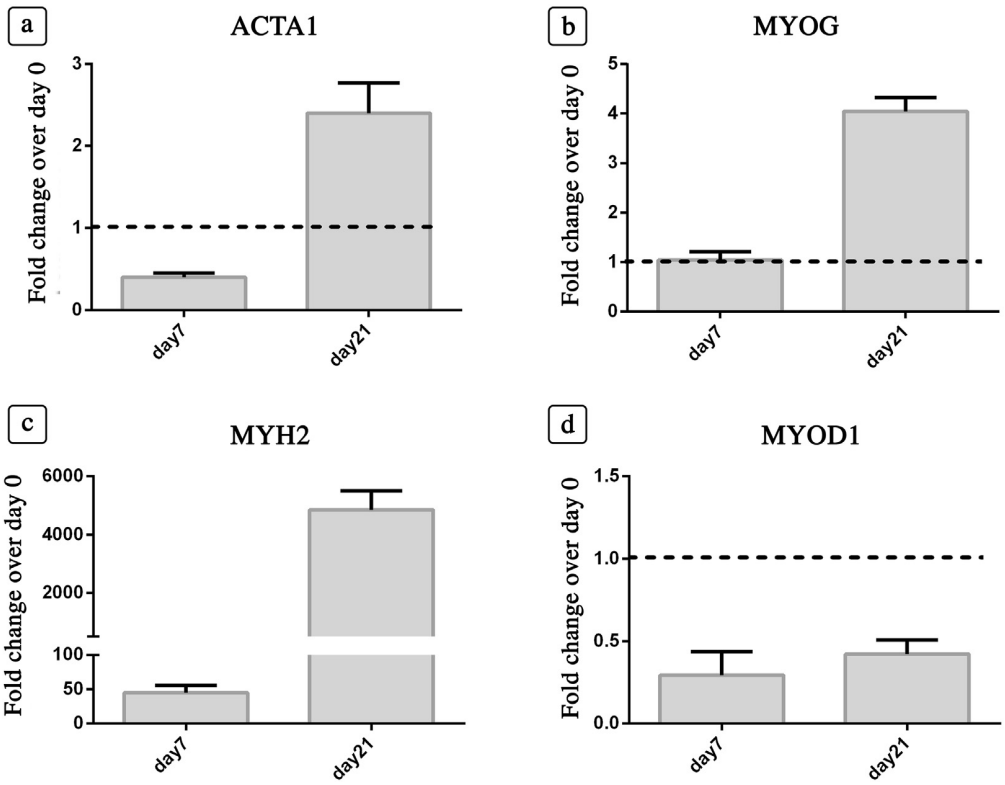

Fig. 5. mRNA expression levels of selected myogenic differentiation markers measured by RT-qPCR for 3D bioprinted constructs at desired time points (7,21 days). Bar charts depict fold change of expression levels normalized to day 0.

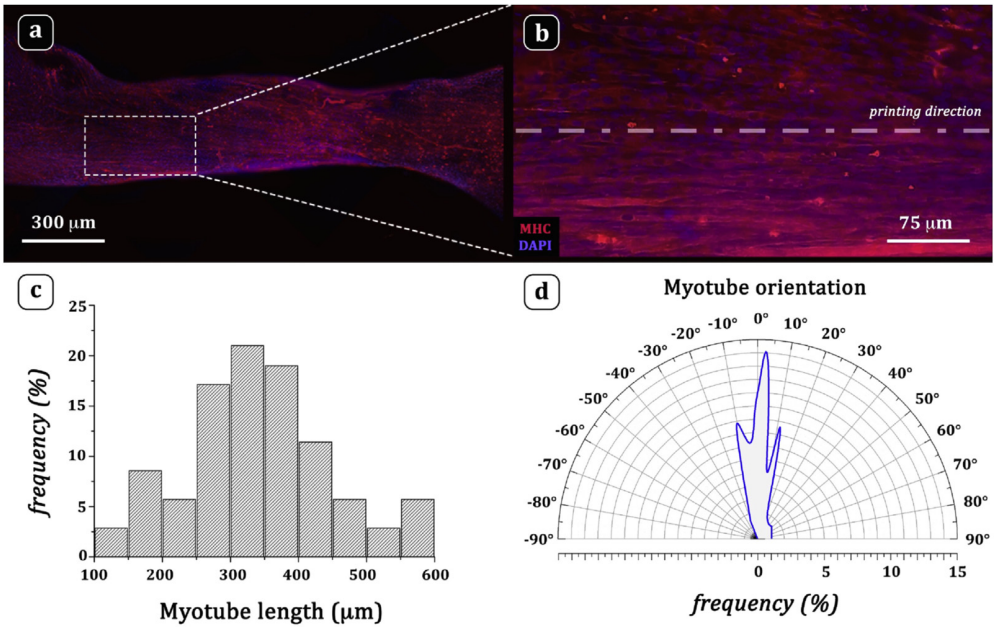

Fig. 6. Quantification of myotube alignment and length in muscle networks obtained in 3D bioprinted constructs after 15 days of *in vitro* culture. a) Tiled immunofluorescence micrographs of a large region (300 × 2000 μm) and b) high magnification of the ROI evidenced in (a). c) Myotube length distribution. d) Polar chart of myotube orientation, with 0° corresponding to the printing direction.

maturation in a small scale *in vitro* [6,40,41]. However, preserving the correct myo-architecture during *in vivo* engraftment still represents a challenge.

Furthermore, as many tissues and organs, skeletal muscle is not assembled from a single cell type and needs blood vessel and nerves for correct functioning. Thus, to further advance skeletal

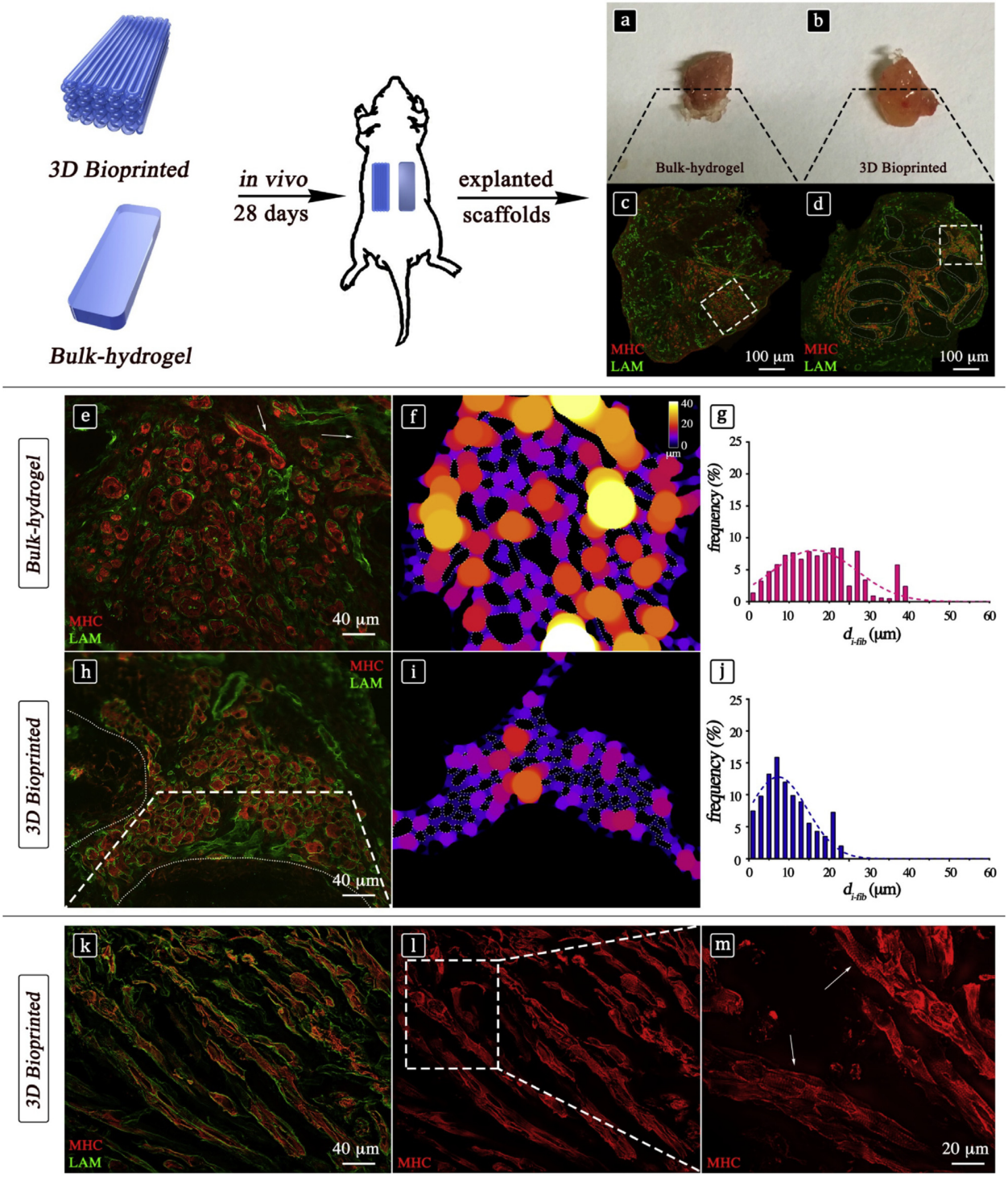

Fig. 7. *In vivo* implantation of PF constructs on the back of immunocompromised SCID mice. a,b) Optical macrographs of the explants after 28 days of *in vivo* culture. c,d) Immunofluorescence micrographs on explant cross-sections stained for MHC (in red) and LAM (in green). e,h) Magnification of the dotted areas in c,d) obtained from bulk-hydrogel (e) and 3D bioprinted (h) explants. f,i) Color-calibrated maps of inter-myofiber spacing ($d_{i\text{-}fib}$) for bulk-hydrogel (f) and 3D bioprinted (i) explants. g,j) Distribution charts from (f,i). k) Longitudinal cross-section of 3D bioprinted explant showing functional organization of MHC and LAM. l) MHC immunostaining reveals fully striated sarcomeric organization in artificial muscle myofibers. m) Magnification of dotted area in (l) favoring sarcomeres identification (white arrows). (For interpretation of the references to colour in this figure legend, the reader is referred to the web version of this article.)

muscle tissue engineering, it is necessary to develop new technologies capable of fabricating 3D engineered constructs with accurate spatial organization of different cell types.

Nowadays, additive manufacturing technologies are revolutionizing all manufacturing fields, including tissue engineering [42]. In particular, 3D bioprinting technologies hold great promise

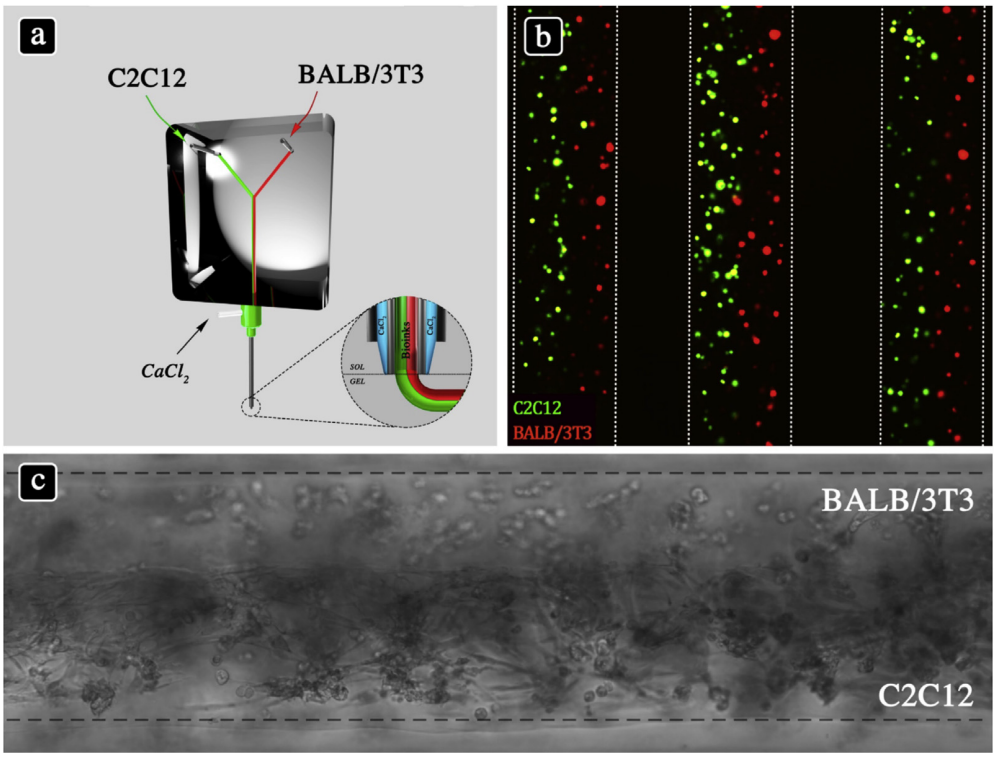

Fig. 8. Multi-cellular 3D bioprinting through a microfluidic printing head. a) C2C12 myogenic precursors and BALB/3T3 fibroblasts were extruded with the same flow rates to obtain a Janus-like compartmentalization within each laid hydrogel fiber. b) C2C12 and BALB/3T3 were respectively infected with GFP (green fluorescent) and mOrange (red fluorescent) lentiviruses for optimal identification following 3D bioprinting. c) Compartmentalization of the two cell types was still retained after 5 days of culture. (For interpretation of the references to colour in this figure legend, the reader is referred to the web version of this article.)

for the rapid and cost-effective production of highly customized and cellularized constructs. These technologies have characteristics that are particularly suitable for the task of assembling *in vitro* artificial muscles. In addition, they are in principle scalable and have the potential to build human-sized myostructures [14,42,43]. However, the accuracy in cell deposition offered by these technologies is still far from that required to mimic the whole native morphology of tissues/organs and, thus, limited tissue/organ functionality can be recapitulated.

To bridge the gap between accessibility and performance, we developed a new concept of extrusion-based bioprinting technique, which implements a microfluidic control in the dispensation of the bioink. An interesting feature offered by our extrusion system is that the accuracy and printing quality are completely decoupled from the rheological behavior of the extruded bioink. This means that the composition of the deposited bioink can be freely tailored by blending ALG with a vast selection of biopolymers—generally photocurable—independently from their rheological properties, opening new routes for the deposition of value-added biopolymers with non-ideal rheological properties [18]. Indeed, in this work we report the successful 3D deposition of PEG-Fibrinogen, a non-easily processable biomaterial. This represents a tremendous advantage, as it has been demonstrated that fibrinogen-derived biomaterials—in addition to their biodegradable nature and non-immunogenicity—support cell adhesion, spreading, and differentiation of several cell lines including muscle progenitors [7,16,32,44–47]. Moreover, the microfluidic printing head, compatible with functional-graded (i.e., multi-material and/or multi-cellular) additive manufacturing might represent an enabling technology for future 4D printing strategies [48].

These features, combined with the tailored bioink composed of PEG-Fibrinogen and alginate, allowed building myoconstructs with different mesh and size bridling myogenic cells (C2C12) and fibroblasts (BALB/3T3) in precise constraints to guide myotube alignment (Figs. 4 and 6, S1, S4). Although recent publications explored 3D printing technology for skeletal muscle tissue engineering [13,14], the results obtained were still unsatisfactory, revealing a poor architectural organization *in vitro* and *in vivo*. On the contrary, in this study we obtained a remarkable muscle structuration not only at the morphological level, but also and overall at the functional level, as the myostructures present sarcomerogenesis and show full functionality (Fig. 4o and Supplementary Video 2). The salient features of our strategy include: i) the small diameter of the deposited fibers (ca. 200 μm vs. >400 μm reported in other studies [13–15]) which better confine C2C12 myoblasts; ii) the inner grid structure composed of tightly packed layers of unidirectionally oriented PF fibers; and iii) the formulation of a unique bioink containing PEG-Fibrinogen, a semi-synthetic polymer able to enhance myogenic differentiation. Hence, 3D bioprinted myostructures were also implanted subcutaneously *in vivo* in the back of immunocompromised mice, revealing the impressive capability to generate a better organized muscle-like tissue compared to bulk hydrogels, and showing complete maturation, as revealed by sarcomerogenesis and full myofiber striation (Fig. 7).

Supplementary video related to this article can be found at http://dx.doi.org/10.1016/j.biomaterials.2017.03.026.

5. Conclusion

We have presented an innovative strategy for 3D printing biomimetic constructs composed of unidirectionally aligned hydrogel fibers loaded with muscle cell precursors (C2C12) in combination

or not with fibroblasts (BALB/3T3). The 3D fabricated samples were tested both *in vitro* and *in vivo* to evaluate their capability of supporting myogenesis and sarcomerogenesis. The results showed that after 21 days of culture *in vitro*, C2C12 properly spread and fused forming highly aligned long-range multinucleated myotubes, with abundant and functional expression of myosin heavy chain (MHC) and laminin (LAM). Besides, the 3D fabricated constructs when grafted *in vivo* led to a substantial improvement—if compared to bulk-hydrogel constructs used as control—of muscle-like architectural organization with the formation of tightly-packed, highly parallel and completely striated myotube fibers. Interestingly, we noticed that 3D bioprinted hydrogel fibers were partially degraded during *in vivo* culture, and started being moderately substituted by the arising myofibers.

Further exploration of multi-material/cellular deposition through our microfluidic printing head will allow us to fabricate more complex engineered constructs that might better recapitulate the whole muscle histoarchitecture *in vitro* and *in vivo*, by including, for example, microvascular networks. Further work will also include the measurement of force generation during contraction under electrical and/or biochemical inducement.

In conclusion, we believe that the described results represent an extraordinary advance in the field of skeletal muscle tissue engineering, providing the chance, in a relatively near future, to reconstruct missing, failing, or damaged muscles parts.

Acknowledgements

This work has been supported in part by grants from the European Research Council (ERC Advanced Grant # 322749/DEPTH to G.C. and Starting Grant # 279647 to P.G.), by Grant #STRATEGMED1/233224/10/NCBR/2014 [project START] to W.S., and by Uncovering Excellence Grant 2014 [MDESMPLAT] and PRIN2015 # 2015FBNB5Y_002 to C.G.

Appendix A. Supplementary data

Supplementary data related to this article can be found at http://dx.doi.org/10.1016/j.biomaterials.2017.03.026.

References

[1] M. Buckingham, D. Montarras, The origin and genetic regulation of myogenic cells: from the embryo to the adult, in: Skelet. Muscle Repair Regen, Springer, Netherlands, Dordrecht, n.d.: pp. 19–44. http://doi.org/10.1007/978-1-4020-6768-6_2.

[2] D.J. Milner, J.A. Cameron, Muscle repair and regeneration: stem cells, scaffolds, and the contributions of skeletal muscle to amphibian limb regeneration, Curr. Top. Microbiol. Immunol. 367 (2013) 133–159, http://dx.doi.org/10.1007/82_2012_292.

[3] J.G. Tidball, Mechanisms of muscle injury, repair, and regeneration, Compr. Physiol. 1 (2011) 2029–2062, http://dx.doi.org/10.1002/cphy.c100092.

[4] P. Heher, B. Maleiner, J. Prüller, A.H. Teuschl, J. Kollmitzer, X. Monforte, S. Wolbank, H. Redl, D. Rünzler, C. Fuchs, A novel bioreactor for the generation of highly aligned 3D skeletal muscle-like constructs through orientation of fibrin via application of static strain, Acta Biomater. 24 (2015) 251–265, http://dx.doi.org/10.1016/j.actbio.2015.06.033.

[5] A. Ito, Y. Yamamoto, M. Sato, K. Ikeda, M. Yamamoto, H. Fujita, E. Nagamori, Y. Kawabe, M. Kamihira, Induction of functional tissue-engineered skeletal muscle constructs by defined electrical stimulation, Sci. Rep. 4 (2014) 4781, http://dx.doi.org/10.1038/srep04781.

[6] L. Madden, M. Juhas, W.E. Kraus, G.A. Truskey, N. Bursac, Bioengineered human myobundles mimic clinical responses of skeletal muscle to drugs, Elife 2015 (2015) 1–14, http://dx.doi.org/10.7554/eLife.04885.

[7] C. Fuoco, R. Rizzi, A. Biondo, E. Longa, A. Mascaro, K. Shapira-Schweitzer, O. Kossovar, S. Benedetti, M.L. Salvatori, S. Santoleri, S. Testa, S. Bernardini, R. Bottinelli, C. Bearzi, S.M. Cannata, D. Seliktar, G. Cossu, C. Gargioli, In vivo generation of a mature and functional artificial skeletal muscle, EMBO Mol. Med. 7 (2015) 411–422, http://dx.doi.org/10.15252/emmm.201404062.

[8] M. Juhas, G.C. Engelmayr, A.N. Fontanella, G.M. Palmer, N. Bursac, Biomimetic engineered muscle with capacity for vascular integration and functional maturation in vivo, Proc. Natl. Acad. Sci. U. S. A. 111 (2014) 5508–5513, http://dx.doi.org/10.1073/pnas.1402723111.

[9] H.H. Vandenburgh, S. Swasdison, P. Karlisch, Computer-aided mechanogenesis of skeletal muscle organs from single cells in vitro, FASEB J. 5 (1991) 2860–2867. http://www.ncbi.nlm.nih.gov/pubmed/1916108.

[10] F.P.W. Melchels, M.A.N. Domingos, T.J. Klein, J. Malda, P.J. Bartolo, D.W. Hutmacher, Additive manufacturing of tissues and organs, Prog. Polym. Sci. 37 (2012) 1079–1104, http://dx.doi.org/10.1016/j.progpolymsci.2011.11.007.

[11] M.M. Stanton, J. Samitier, S. Sánchez, Bioprinting of 3D hydrogels, Lab. Chip 15 (2015) 3111–3115, http://dx.doi.org/10.1039/C5LC90069G.

[12] F. Pati, J. Jang, D.-H. Ha, S. Won Kim, J.-W. Rhie, J.-H. Shim, D.-H. Kim, D.-W. Cho, Printing three-dimensional tissue analogues with decellularized extracellular matrix bioink, Nat. Commun. 5 (2014) 3935, http://dx.doi.org/10.1038/ncomms4935.

[13] Y.-J. Choi, T.G. Kim, J. Jeong, H.-G. Yi, J.W. Park, W. Hwang, D.-W. Cho, 3D cell printing of functional skeletal muscle constructs using skeletal muscle-derived bioink, Adv. Healthc. Mater. (2016) 1–10, http://dx.doi.org/10.1002/adhm.201600483.

[14] H.-W. Kang, S.J. Lee, I.K. Ko, C. Kengla, J.J. Yoo, A. Atala, A 3D bioprinting system to produce human-scale tissue constructs with structural integrity, Nat. Biotechnol. (2016), http://dx.doi.org/10.1038/nbt.3413.

[15] T.K. Merceron, M. Burt, Y.-J. Seol, H.-W. Kang, S.J. Lee, J.J. Yoo, A. Atala, A 3D bioprinted complex structure for engineering the muscle–tendon unit, Biofabrication 7 (2015) 35003, http://dx.doi.org/10.1088/1758-5090/7/3/035003.

[16] L. Almany, D. Seliktar, Biosynthetic hydrogel scaffolds made from fibrinogen and polyethylene glycol for 3D cell cultures, Biomaterials 26 (2005) 2467–2477, http://dx.doi.org/10.1016/j.biomaterials.2004.06.047.

[17] C. Colosi, S.R. Shin, V. Manoharan, S. Massa, M. Costantini, A. Barbetta, M.R. Dokmeci, M. Dentini, A. Khademhosseini, Microfluidic bioprinting of heterogeneous 3D tissue constructs using low-viscosity bioink, Adv. Mater. 28 (2016) 677–684, http://dx.doi.org/10.1002/adma.201503310.

[18] M. Costantini, J. Idaszek, K. Szöke, J. Jaroszewicz, M. Dentini, A. Barbetta, J.E. Brinchmann, W. Święszkowski, 3D bioprinting of BM-MSCs-loaded ECM biomimetic hydrogels for in vitro neocartilage formation, Biofabrication 8 (2016) 35002, http://dx.doi.org/10.1088/1758-5090/8/3/035002.

[19] J. Schindelin, C.T. Rueden, M.C. Hiner, K.W. Eliceiri, The ImageJ ecosystem: an open platform for biomedical image analysis, Mol. Reprod. Dev. 82, (n.d.), 518–529. http://doi.org/10.1002/mrd.22489.

[20] R. Scardigli, C. Gargioli, D. Tosoni, U. Borello, M. Sampaolesi, C. Sciorati, S. Cannata, E. Clementi, S. Brunelli, G. Cossu, Binding of sFRP-3 to EGF in the extra-cellular space affects proliferation, differentiation and morphogenetic events regulated by the two molecules, PLoS One 3 (2008) e2471, http://dx.doi.org/10.1371/journal.pone.0002471.

[21] J. Vandesompele, K. De Preter, F. Pattyn, B. Poppe, N. Van Roy, A. De Paepe, F. Speleman, Accurate normalization of real-time quantitative RT-PCR data by geometric averaging of multiple internal control genes, Genome Biol. 3 (2002). RESEARCH0034. http://www.ncbi.nlm.nih.gov/pubmed/12184808.

[22] C. Colosi, M. Costantini, A. Barbetta, R. Pecci, R. Bedini, M. Dentini, Morphological comparison of PVA scaffolds obtained by gas foaming and microfluidic foaming techniques, Langmuir 29 (2013) 82–91, http://dx.doi.org/10.1021/la303788z.

[23] R.R. Jose, M.J. Rodriquez, T.A. Dixon, F.G. Omenetto, D.L. Kaplan, Evolution of bioinks and additive manufacturing technologies for 3D bioprinting, ACS Biomater. Sci. Eng. 2 (2016) 1662–1678, http://dx.doi.org/10.1021/acsbiomaterials.6b00088.

[24] J. Malda, J. Visser, F.P. Melchels, T. Jüngst, W.E. Hennink, W.J.A. Dhert, J. Groll, D.W. Hutmacher, 25th anniversary article: engineering hydrogels for biofabrication, Adv. Mater. 25 (2013) 5011–5028, http://dx.doi.org/10.1002/adma.201302042.

[25] C. Colosi, M. Costantini, R. Latini, S. Ciccarelli, A. Stampella, A. Barbetta, M. Massimi, L. Conti Devirgiliis, M. Dentini, Rapid prototyping of chitosan-coated alginate scaffolds through the use of a 3D fiber deposition technique, J. Mater. Chem. B 2 (2014) 6779–6791, http://dx.doi.org/10.1039/C4TB00732H.

[26] R. Lapasin, S. Pricl, Rheology of Industrial Polysaccharides: Theory and Applications, Springer, US, Boston, MA, 1995, http://dx.doi.org/10.1007/978-1-4615-2185-3.

[27] L.E. Bertassoni, J.C. Cardoso, V. Manoharan, A.L. Cristino, N.S. Bhise, W.A. Araujo, P. Zorlutuna, N.E. Vrana, A.M. Ghaemmaghami, M.R. Dokmeci, A. Khademhosseini, Direct-write bioprinting of cell-laden methacrylated gelatin hydrogels, Biofabrication 6 (2014) 24105, http://dx.doi.org/10.1088/1758-5082/6/2/024105.

[28] L. Sun, S.T. Parker, D. Syoji, X. Wang, J.A. Lewis, D.L. Kaplan, Direct-Write assembly of 3D silk/hydroxyapatite scaffolds for bone Co-Cultures, Adv. Healthc. Mater. 1 (2012) 729–735, http://dx.doi.org/10.1002/adhm.201200057.

[29] K. Tanaka, K. Sato, T. Yoshida, T. Fukuda, K. Hanamura, N. Kojima, T. Shirao, T. Yanagawa, H. Watanabe, Evidence for cell density affecting C2C12 myogenesis: possible regulation of myogenesis by cell-cell communication, Muscle Nerve 44 (2011) 968–977, http://dx.doi.org/10.1002/mus.22224.

[30] A.J. Engler, M.A. Griffin, S. Sen, C.G. Bönnemann, H.L. Sweeney, D.E. Discher, Myotubes differentiate optimally on substrates with tissue-like stiffness: pathological implications for soft or stiff microenvironments, J. Cell Biol. 166 (2004) 877–887, http://dx.doi.org/10.1083/jcb.200405004.

[31] A.J. Engler, S. Sen, H.L. Sweeney, D.E. Discher, Matrix elasticity directs stem cell lineage specification, Cell 126 (2006) 677–689, http://dx.doi.org/10.1016/

j.cell.2006.06.044.
[32] C. Fuoco, M.L. Salvatori, A. Biondo, K. Shapira-Schweitzer, S. Santoleri, S. Antonini, S. Bernardini, F.S. Tedesco, S. Cannata, D. Seliktar, G. Cossu, C. Gargioli, Injectable polyethylene glycol-fibrinogen hydrogel adjuvant improves survival and differentiation of transplanted mesoangioblasts in acute and chronic skeletal-muscle degeneration, Skelet. Muscle 2 (2012) 24, http://dx.doi.org/10.1186/2044-5040-2-24.
[33] S.T. Cooper, A.L. Maxwell, E. Kizana, M. Ghoddusi, E.C. Hardeman, I.E. Alexander, D.G. Allen, K.N. North, C2C12 co-culture on a fibroblast substratum enables sustained survival of contractile, highly differentiated myotubes with peripheral nuclei and adult fast myosin expression, Cell Motil. Cytoskelet. 58 (2004) 200–211, http://dx.doi.org/10.1002/cm.20010.
[34] I.Y. Shadrin, A. Khodabukus, N. Bursac, Striated muscle function, regeneration, and repair, Cell. Mol. Life Sci. 73 (2016) 4175–4202, http://dx.doi.org/10.1007/s00018-016-2285-z.
[35] C. Fuoco, L.L. Petrilli, S. Cannata, C. Gargioli, Matrix scaffolding for stem cell guidance toward skeletal muscle tissue engineering, J. Orthop. Surg. Res. 11 (2016) 86, http://dx.doi.org/10.1186/s13018-016-0421-y.
[36] C. Fuoco, S. Cannata, C. Gargioli, Could a functional artificial skeletal muscle be useful in muscle wasting? Curr. Opin. Clin. Nutr. Metab. Care 19 (2016) 182–187, http://dx.doi.org/10.1097/MCO.0000000000000271.
[37] B.M. Sicari, J.P. Rubin, C.L. Dearth, M.T. Wolf, F. Ambrosio, M. Boninger, N.J. Turner, D.J. Weber, T.W. Simpson, A. Wyse, E.H.P. Brown, J.L. Dziki, L.E. Fisher, S. Brown, S.F. Badylak, An acellular biologic scaffold promotes skeletal muscle formation in mice and humans with volumetric muscle loss, Sci. Transl. Med. 6 (2014) 234ra58, http://dx.doi.org/10.1126/scitranslmed.3008085.
[38] M.A. Machingal, B.T. Corona, T.J. Walters, V. Kesireddy, C.N. Koval, A. Dannahower, W. Zhao, J.J. Yoo, G.J. Christ, A tissue-engineered muscle repair construct for functional restoration of an irrecoverable muscle injury in a murine model, Tissue Eng. Part A 17 (2011) 2291–2303, http://dx.doi.org/10.1089/ten.TEA.2010.0682.
[39] S. Levenberg, J. Rouwkema, M. Macdonald, E.S. Garfein, D.S. Kohane, D.C. Darland, R. Marini, C.A. van Blitterswijk, R.C. Mulligan, P.A. D'Amore, R. Langer, Engineering vascularized skeletal muscle tissue, Nat. Biotechnol. 23 (2005) 879–884, http://dx.doi.org/10.1038/nbt1109.
[40] P. Heher, B. Maleiner, J. Prüller, A.H. Teuschl, J. Kollmitzer, X. Monforte, S. Wolbank, H. Redl, D. Rünzler, C. Fuchs, A novel bioreactor for the generation of highly aligned 3D skeletal muscle-like constructs through orientation of fibrin via application of static strain, Acta Biomater. 24 (2015) 251–265, http://dx.doi.org/10.1016/j.actbio.2015.06.033.
[41] M. Juhas, G.C. Engelmayr, A.N. Fontanella, G.M. Palmer, N. Bursac, Biomimetic engineered muscle with capacity for vascular integration and functional maturation in vivo, Proc. Natl. Acad. Sci. U. S. A. 111 (2014) 5508–5513, http://dx.doi.org/10.1073/pnas.1402723111.
[42] S.V. Murphy, A. Atala, 3D bioprinting of tissues and organs, Nat. Biotechnol. 32 (2014) 773–785, http://dx.doi.org/10.1038/nbt.2958.
[43] V. Mironov, V. Kasyanov, C. Drake, R.R. Markwald, Organ printing: promises and challenges, Regen. Med. 3 (2008) 93–103, http://dx.doi.org/10.2217/17460751.3.1.93.
[44] C. Fuoco, E. Sangalli, R. Vono, S. Testa, B. Sacchetti, M.V.G. Latronico, S. Bernardini, P. Madeddu, G. Cesareni, D. Seliktar, R. Rizzi, C. Bearzi, S.M. Cannata, G. Spinetti, C. Gargioli, 3D hydrogel environment rejuvenates aged pericytes for skeletal muscle tissue engineering, Front. Physiol. 5 (2014) 203, http://dx.doi.org/10.3389/fphys.2014.00203.
[45] P. Kerscher, I.C. Turnbull, A.J. Hodge, J. Kim, D. Seliktar, C.J. Easley, K.D. Costa, E.A. Lipke, Direct hydrogel encapsulation of pluripotent stem cells enables ontomimetic differentiation and growth of engineered human heart tissues, Biomaterials 83 (2016) 383–395, http://dx.doi.org/10.1016/j.biomaterials.2015.12.011.
[46] K. Shapira-Schweitzer, M. Habib, L. Gepstein, D. Seliktar, A photopolymerizable hydrogel for 3-D culture of human embryonic stem cell-derived cardiomyocytes and rat neonatal cardiac cells, J. Mol. Cell. Cardiol. 46 (2009) 213–224, http://dx.doi.org/10.1016/j.yjmcc.2008.10.018.
[47] M. Centola, F. Abbruzzese, C. Scotti, A. Barbero, G. Vadalà, V. Denaro, I. Martin, M. Trombetta, A. Rainer, A. Marsano, Scaffold-based delivery of a clinically relevant anti-angiogenic drug promotes the formation of *in vivo* stable cartilage, Tissue Eng. Part A 19 (2013) 1960–1971, http://dx.doi.org/10.1089/ten.tea.2012.0455.
[48] J. Choi, O.C. Kwon, W. Jo, H.J. Lee, M.W. Moon, 4D printing technology: a review, 3d Print. Addit. Manuf. 2 (2015) 159–167, http://dx.doi.org/10.1089/3dp.2015.0039.